PERGAMON

International Journal of Heat and Mass Transfer 45 (2002) 4493–4505

International Journal of HEAT and MASS TRANSFER

www.elsevier.com/locate/ijhmt

Numerical simulation of turbulent flow field and heat transfer in a two-dimensional channel with periodic slit ribs

Tong-Miin Liou *, Shih-Hui Chen, Kuan-Chen Shih

Department of Power Mechanical Engineering, National Tsing Hua University, No. 101, Sec. 2, Kuang-Fu Road, Hsinchu 30013, Taiwan, ROC

Received 24 January 2002; received in revised form 8 April 2002

Abstract

Spatially periodic turbulent fluid flow and heat transfer in a channel with slit rectangular ribs mounted on one wall have been numerically investigated. A Reynolds stress model with wall function and a modified wall-related pressure-strain model for reducing the overestimation of turbulent kinetic energy at impingement/reattachment region was employed in the two-dimensional simulation. QUICK discretization scheme and nonstaggered grid system were used. The parameters fixed were rib height-to-duct height ratio of 0.17, rib width-to-height ratio of 0.76, rib pitch-to-height ratio of 10, and Reynolds number based on channel hydraulic diameter and bulk mean velocity of 2×10^4, while the main parameter varied was the rib open-area ratio with values of $\beta = 0\%$, 10%, 22%, 32%, and 44%. Two critical ranges of β and three characteristic flow regimes are identified, which is similar to the experimental results reported by previous researchers for the hole-type perforated ribs except a smaller critical β for impermeability. The rationale for the difference in the critical β between the slit-type and hole-type perforated ribs is addressed in terms of effective pore diameters. From the variations of the friction loss, convective mean velocity, turbulent kinetic energy, and negative pressure behind the perforated ribs with β, that $\beta = 44\%$ attains the best thermal performance $\overline{Nu}_p/\overline{Nu}_s^*$ under the constant pumping power condition is unraveled. A comparison of $\overline{Nu}_p/\overline{Nu}_s^*$ distributions between vertical-slit ribs measured by other research groups and horizontal-slit ribs computed presently is also made.

1. Introduction

The use of rough or extended surfaces is the most common one of the passive methods for heat transfer augmentation. Among the various devices, pipes or ducts with transverse ribs placed at regular intervals are often adopted. In spite of the increase in the heat transfer rate of the ribbed channels, the pressure loss is also increased. Moreover, local heat transfer deterioration is usually associated with the presence of the recirculation zone immediately behind the rib. To remove the recirculation zone and hence the local heat transfer deterioration in the rib-wall corners of the attached solid ribs, permeable ribs, including porous [1], slit [2], and hole-type [3] perforated ribs, are among those of promising choices. A channel with permeable ribs leads to a flowfield characterized by having fluid flow partially through and partially around the ribs. The present study aims for simulating such a complex turbulent flow.

Among previous studies of turbulent flows around perforated bluff bodies in a rectangular channel, Tanasawa et al. [4] employed the resistance heating method and thermocouple technique to determine the heat transfer coefficients in a channel with perforated plates of fence-type, hole-type, and slit-type symmetrically mounted on two opposite walls for plate open area ratio β (defined in Fig. 1) and Reynolds number Re ranging from 0% to 50%, and 1.3×10^4 to 9×10^4, respectively. Results showed that surfaces with hole-type perforated plates gave excellent performance under the same pumping power. Under the same flow conditions,

* Corresponding author. Tel.: +886-3-5742607; fax: +886-3-5729716.

E-mail address: tmliou@pme.nthu.edu.tw (T.-M. Liou).

0017-9310/02/$ - see front matter
PII: S0017-9310(02)00157-6

Nomenclature

B	half height of channel (m)
C_p	pressure coefficient $= (p - p_{\text{ref}})/(0.5\rho U_{\text{b}}^2)$, where p_{ref} is the outlet pressure
De	duct hydraulic diameter, $4B$ (m)
f	(Darcy) friction factor; the wall-proximity function
h	local heat transfer coefficient $= q_{\text{w}}/(T_{\text{w}} - T_{\text{b}})$ (Watt/m^2 K)
H	rib (cylinder) height (m)
k	turbulent kinetic energy (m^2/s^2)
k_{f}	thermal conductivity of fluid (Watt/m K)
L_{R}	length of primary recirculation zone, mean reattachment length, wake length (m)
$\dot{m}$	channel flow rate (m^3/s)
N	total number of perforations drilled through the rib
Nu	local Nusselt number $= (h\text{De}/k_{\text{f}})$
$\overline{Nu}_{\text{s}}^*$	average Nusselt number for the smooth duct (at the same pumping power)
$\overline{Nu}_{\text{p}}$	pitch-average Nusselt number for a ribbed channel, including the outer surfaces of the rib and the floor region between the consecutive ribs
p	pressure (N/m^2)
$\hat{p}$	transformed pressure
Pi	rib pitch (m)
PR	rib pitch-to-rib height ratio $= \text{Pi}/H$
q_{w}	local wall heat flux (W/m^2)
r	space coordinate
Re	Reynolds number based on channel hydraulic diameter ($\equiv \rho U_{\text{ref}}\text{De}/\mu$)
S_{p}	stagnation-point distance (m)
T	temperature (K)
T_{b}	local bulk mean temperature $= \int_0^B \lvert u\rvert T\,\text{d}Y / \int_0^B \lvert u\rvert\,\text{d}Y$
T_{w}	local wall temperature (K)
t	time coordinate (s)
$\hat{T}$	transformed temperature
u	streamwise Cartesian velocity (m/s)
U_{b}	duct bulk mean velocity (m/s)
$\langle u\rangle_{\text{t}}$	long-time mean streamwise velocity (m/s)
U_{ref}	duct bulk mean velocity (U_{b}) as a reference velocity (m/s)
U_{mn}	maximum negative streamwise mean velocity (m/s)
v	transverse Cartesian velocity (m/s)
$\langle v\rangle_{\text{t}}$	long-time mean transverse velocity (m/s)
W_{r}	rib width (m)
X	streamwise coordinate
X_{J}	effective jet length (m)
X_{R}	reattachment length (m)
Y	transverse coordinate
y^+	dimensionless distance from walls $= Yu_\tau/v$
Z	spanwise coordinate

Greek symbols

β	open-area ratio of perforated or slit rib, $(N\pi\varphi^2)/(2AH)$
δ_{ij}	Kronecker delta function
γ	the temperature increase parameter $= (T(X + \text{Pi}, Y) - T(X, Y))/\text{Pi}$
ε	dissipation rate of turbulence kinetic energy (m^2/s^3)
κ	the von Karman constant ($= 0.418$)
λ	the pressure drop parameter $= [p(X, Y) - p(X + \text{Pi}, Y)]/\text{Pi}$
μ	dynamic viscosity (kg/m s)
μ_{t}	turbulent (eddy) dynamic viscosity (kg/m s)
ν	kinematic viscosity (m^2/s)
ν_{t}	turbulent (eddy) kinematic viscosity (m^2/s)
ρ	fluid density (kg/m^3)
σ	turbulent Prandtl number
τ	viscous shear stress (N/m^2)
τ_{w}	shear stress at wall (N/m^2)
φ	the radius of perforation
Ψ	stream function
$\phi_{ij\text{w}}$	wall-related pressure strain term in Reynolds stress model

Subscripts

e	exit plane
w	wall

Tanasawa et al. [5] subsequently compared the thermal performances of plain rectangular ribs, hole-type perforated ribs, and hole-type half-perforated ribs. They concluded that hole-type half-perforated rib with perforations on the lower half of the rib gave better performance. Another important finding was that the local heat transfer coefficient decreased as a whole when fewer than two pairs of ribs were placed upstream. Ichimiya and Mitsushiro [6] studied the effect of rib thickness, $W_{\text{r}}/H = 0.5$, 1, and 1.5, on the thermal performance and friction loss of flow in a rectangular duct with porous-type ribs arranged on one insulated wall placed opposite to the smooth heated wall for rib pitch-to-height ratio of $\text{Pi}/H = 3.5$, rib open area ratio of $\beta = 87.3\%$, and Reynolds number of $Re = 2.6 \times 10^4$–1.5×10^5. The thermocouple measured average Nusselt number and pressure tap measured average friction factor were respectively found to be augmented to about two to four

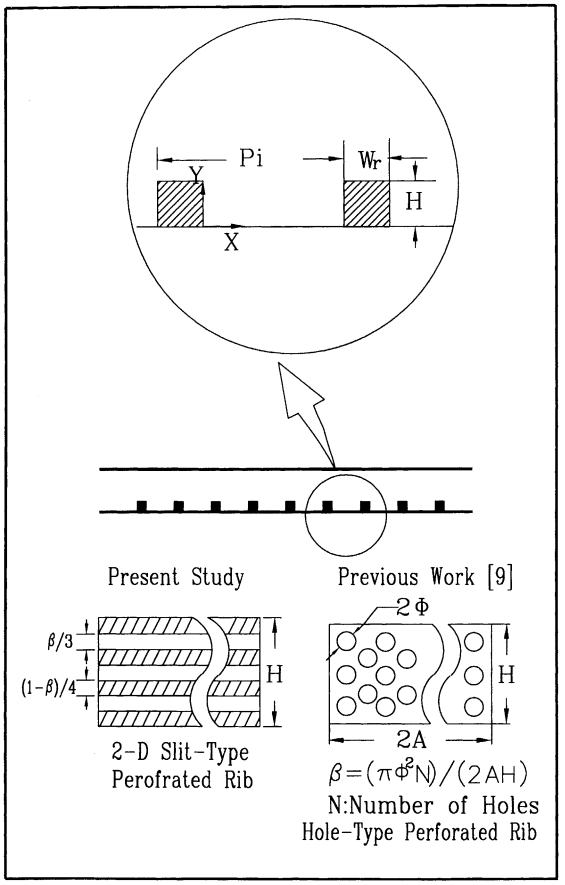

Fig. 1. Sketch of configuration for 2-D channel with periodically permeable ribs.

times that of the smooth duct and reduced to one-fourth to two-thirds of that of the solid-type ribs. Nevertheless, no conclusive trend for rib-thickness effect was reported. Ichimiya et al. [7] further experimentally investigated the effects of a single porous-type roughness of $\beta = 87.3\%$ on the heat transfer and friction characteristics in a parallel plate duct. The porous-type roughness was applied to the insulated wall facing the heated smooth surface. Results showed that the thermal performance under the constant pumping power constraint is better in the laminar region than in the turbulent region. Yamada and Osaka [8] conducted flow visualization and pressure measurements to study the effects of the aspect ratio and open-area ratio of the plate on the heat transfer characteristics of the flow over a rectangular hole-type perforated plate standing on a flat wall. Only one flow velocity ($U_b = 5$ m/s) was tested. They found that the critical open-area ratios for the presence of a recirculation behind the plate were between 32.5% and 48.5%. Hwang and Liou [3] focused on the heat transfer enhancement in a channel containing hole-type perforated ribs. The experimental techniques employed were laser holographic interferometry and Pitot tube, and the parameters investigated were rib open-area ratio ($\beta = 0$–44%), rib pitch-to-height ratio ($\mathrm{Pi}/H = 5$–10), and rib height-to-channel hydraulic diameter ratio ($H/\mathrm{De} = 0.081$–0.162). An important finding they made was that the ribs with $\beta = 44\%$ gave the best thermal performance among the rib open area ratios investigated. Liou et al. [9] undertook the velocity field measurements for a hole-type perforated rib array mounted on one wall of a rectangular duct by using nonintrusive laser-Doppler velocimetry. The size of holes is varied to examine its effect on the flow structures. In addition, the acquired fluid flow information was used to illustrate the previous heat transfer results [3]. Hwang [10] investigated the effect of porous-type baffles on heat transfer and friction in a baffled channel. The porous-type baffles were arranged on the bottom and top channel walls in a staggered manner. One porosity of 42% was studied. The porous-type baffle was made of sintered bronze beads with a mean diameter of 0.72 mm. The main finding was that the porous-type-baffled channel yielded a better thermal performance than solid-type-baffled channel. Hwang [2] also studied the fully developed heat transfer and friction characteristics in rectangular ducts with one wall roughened by slit ribs. Three porosities, 19%, 32%, and 48%, were examined. Detailed local Nusselt number distribution was not shown. Only average rib, floor (area between two ribs), and overall heat transfer coefficients were reported. Two contributive factors of heat transfer promotion, namely, the fin effect and the enhanced turbulence effect, were isolated by separately measuring the floor and rib heat transfer.

In the papers cited above, most studies of the turbulent fluid flow and heat transfer in a channel with perforated or porous ribs have so far been experimental. Little attention has been given to the relevant computational simulations. The present work therefore focuses on the corresponding turbulent flow and heat transfer simulation. The calculated results are compared to those of the experiments [3,4,9]. Ribs of slit configuration with the same rib open-area ratio as the hole-type perforated ribs used in the previous measurements were examined in the simulation. The rib open-area ratio was varied among 0, 0.10, 0.22, 0.32, and 0.44.

2. Theoretical analysis

2.1. Governing equations

The time-dependent Navier–Stokes equations and energy equation for an incompressible fluid take the form

$$\frac{\partial u_i}{\partial x_i} = 0 \tag{1}$$

$$\frac{\partial u_i}{\partial t}+\frac{\partial}{\partial x_j}(u_j u_i)=-\frac{\partial p}{\partial x_i}+\nu\frac{\partial}{\partial x_j}\left(\frac{\partial u_i}{\partial x_j}\right) \tag{2}$$

$$\frac{\partial T}{\partial t}+\frac{\partial}{\partial x_j}(u_j T)=\frac{\nu}{Pr}\frac{\partial}{\partial x_j}\left(\frac{\partial T}{\partial x_j}\right) \tag{3}$$

Because of the periodic nature of the flow and temperature field, the pressure p and temperature T can be expressed as

$$\begin{aligned} p(X,Y,Z)&=-\lambda X+\hat{p}(X,Y,Z)\\ T(X,Y,Z)&=\gamma X+\widehat{T}(X,Y,Z)\end{aligned} \tag{4}$$

where the pressure drop parameter $\lambda=(p(X,Y,Z)-p(X+\mathrm{Pi},Y,Z))/\mathrm{Pi}$ and the temperature increase parameter $\gamma=(T(X+\mathrm{Pi},Y,Z)-T(X,Y,Z))/\mathrm{Pi}$ are constants [11]. The term $-\lambda X$ is related to the global mass flow $\dot{m}$ (or Reynolds number) and represents the general decrease in pressure in the streamwise direction. For the case of heating, it can be shown that $\gamma=Q''/(\dot{m}C_p\mathrm{Pi})$ in which Q'' is the rate of heat addition (per unit span) to the fluid in a pitch (Pi). The function $\hat{p}(X,Y,Z)$ and $\widehat{T}(X,Y,Z)$ identically repeat themselves from pitch to pitch and indicate the local departure of pressure and temperature from the linear decay $-\lambda X$ and linear increase X, respectively.

Eqs. (1)–(3) for periodic fully developed flow can be expressed as follows:

$$\frac{\partial u_i}{\partial x_i}=0 \tag{5}$$

$$\frac{\partial u_i}{\partial t}+\frac{\partial}{\partial x_j}(u_j u_i)=-\frac{\partial \hat{p}}{\partial x_i}+\nu\frac{\partial}{\partial x_j}\left(\frac{\partial u_i}{\partial x_j}\right)+\lambda\delta_{i1} \tag{6}$$

$$\frac{\partial \widehat{T}}{\partial t}+\frac{\partial}{\partial x_j}(u_j\widehat{T})=\frac{\nu}{Pr}\frac{\partial}{\partial x_j}\left(\frac{\partial \widehat{T}}{\partial x_j}\right)-\gamma u_i\delta_{i1} \tag{7}$$

For a Reynolds-averaged Navier–Stokes and energy equations, the Reynolds averaging are applied. Following the original idea of Reynolds [12], the variable f is resolved into a mean value $\langle f\rangle$ defined by

$$\langle f\rangle(\vec{r})=\frac{1}{T}\int_{t_0}^{t_0+T} f(\vec{r},t')\,\mathrm{d}t',$$

where $\vec{r}$ is the space vector and a fluctuating value f', $f=\langle f\rangle+f'$, where T is large compared to the relevant period of the fluctuations. The mean value $\langle f\rangle$ itself may vary slowly with time, as in the case of an unsteady turbulent flow involving vortex shedding.

$$\frac{\partial\langle u_i\rangle}{\partial x_i}=0 \tag{8}$$

$$\frac{\partial\langle u_i\rangle}{\partial t}+\frac{\partial}{\partial x_j}\left(\langle u_j\rangle\langle u_i\rangle\right)=-\frac{\partial\langle\hat{p}\rangle}{\partial x_i}+\nu\frac{\partial}{\partial x_j}\left(\frac{\partial\langle u_i\rangle}{\partial x_j}\right)+\lambda\delta_{i1}+\frac{\partial}{\partial x_j}(\tau_{ij}) \tag{9}$$

$$\frac{\partial\langle\widehat{T}\rangle}{\partial t}+\frac{\partial}{\partial x_j}\left(\langle u_j\rangle\langle\widehat{T}\rangle\right)=\frac{\nu}{Pr}\frac{\partial}{\partial x_j}\left(\frac{\partial\left\langle\widehat{T}\right\rangle}{\partial x_j}\right)-\gamma\langle u_i\rangle\delta_{i1}+\frac{\partial}{\partial x_j}(q_j) \tag{10}$$

For phase-averaged Navier–Stokes and energy equations [13,14], the average value $\langle f\rangle$ is varying with time and can be further written as

$$\langle f\rangle=\langle f\rangle_{\mathrm{t}}+\tilde{f}$$

Thus $\langle f\rangle$ is the sum of the long-time-mean value $\langle f\rangle_{\mathrm{t}}$ and the deviation $\tilde{f}$ from $\langle f\rangle_{\mathrm{t}}$.

2.2. Turbulence models

The turbulent stress and heat flux in Eqs. (9) and (10) must be modeled to close the governing equations. The transport equations for the Reynolds stresses can be written in the following Cartesian tensor form [15]:

$$\frac{\partial\langle u_i'u_j'\rangle}{\partial t}+\frac{\partial}{\partial x_k}\left(\langle u_k\rangle\langle u_i'u_j'\rangle\right)=D_{ij}+P_{ij}+\phi_{ij}-\frac{2}{3}\delta_{ij}\varepsilon \tag{11}$$

in which

$$D_{ij}=\frac{\partial}{\partial x_k}\left(c_\mu\frac{\langle k\rangle^2}{\langle\varepsilon\rangle}\frac{\partial\langle u_i'u_j'\rangle}{\partial x_k}\right) \tag{12}$$

$$P_{ij}=-\left(\langle u_i'u_k'\rangle\frac{\partial\langle u_j\rangle}{\partial x_k}+\langle u_i'u_k'\rangle\frac{\partial\langle u_j\rangle}{\partial x_k}\right) \tag{13}$$

$$\phi_{ij}=-c_1\frac{\langle\varepsilon\rangle}{\langle k\rangle}\left(\langle u_i'u_j'\rangle-\frac{2}{3}\delta_{ij}\langle k\rangle\right)-c_2\left(P_{ij}-\frac{1}{3}\delta_{ij}P_k\right)+\phi_{ij}^{\mathrm{wall}} \tag{14}$$

are respectively the diffusion, production, and pressure strain terms.

A modified wall-related pressure-strain model [16], which avoids the inappropriate near-wall enhancement of isotropisation at impingement/reattachment regions as associated with the standard k–ϵ model, is adopted here.

$$\begin{aligned}\phi_{ij}^{\mathrm{wall}}=&\left(c_1'\frac{\langle\varepsilon\rangle}{\langle k\rangle}\langle u_i'u_j'\rangle n_k n_m\delta_{ij}-\frac{3}{2}\langle u_i'u_k'\rangle n_j n_k-\frac{3}{2}\langle u_j'u_k'\rangle n_i n_k\right)\\ &\times f-\left(c_2'\langle u_k'u_m'\rangle+c_3'kn_k n_m\right)\frac{\partial\langle u_k\rangle}{\partial x_m}(n_q n_q\delta_{ij}-3n_k n_m)\\ &\times f-c_4'\left(\tilde{\phi}_{km}n_k n_m\delta_{ij}-\frac{3}{2}\tilde{\phi}_{ik}n_j n_m-\frac{3}{2}\tilde{\phi}_{ik}n_j n_m\right)\end{aligned} \tag{15}$$

where n_i is the unit vector component in the x_i direction and the wall-proximity function $f=(c_\mu^{0.75}\langle k\rangle^{1.5})/(\varepsilon\kappa\Delta n)$ with Δn being the normal distance from the wall. In the Eq. (15), $\tilde{\phi}_{ij}$ takes the following form:

$$\tilde{\phi}_{ij} = \left(\langle u_i' u_k' \rangle - \frac{2}{3}\delta_{ik}\langle k \rangle \right) \frac{\partial \langle u_j \rangle}{\partial x_k} \tag{16}$$
$$c_1' = 0.5, \quad c_2' = 0.08, \quad c_3' = 0.13, \quad c_4' = 0.10$$

The k–ε model is used in connection with wall functions to determine the Reynolds stresses $\langle u_i' u_j' \rangle$. The eddy viscosity concept is adopted to relate the eddy viscosity $\langle v_t \rangle$ to the turbulent kinetic energy $\langle k \rangle$ and its rate of dissipation $\langle \varepsilon \rangle$, i.e., $\langle v_t \rangle = c_\mu \langle k \rangle^2 / \langle \varepsilon \rangle$

The equations for $\langle k \rangle$ and $\langle \varepsilon \rangle$ are given as

$$\frac{\partial \langle k \rangle}{\partial t} + \frac{\partial}{\partial x_j}\left(\langle u_j \rangle \langle k \rangle \right) = D_k + P_k - \langle \varepsilon \rangle = \frac{\partial}{\partial x_j}\left[\left(v + \frac{\langle v_t \rangle}{\sigma_k} \right) \left(\frac{\partial \langle k \rangle}{\partial x_j} \right) \right] + P_k - \langle \varepsilon \rangle \tag{17}$$

$$\frac{\partial \langle \varepsilon \rangle}{\partial t} + \frac{\partial}{\partial x_j}\left(\langle u_j \rangle \langle \varepsilon \rangle \right) = D_\varepsilon + \frac{\langle \varepsilon \rangle}{\langle k \rangle}\left(C_1 P_k - C_2 \langle \varepsilon \rangle \right) = \frac{\partial}{\partial x_j}\left[\left(v + \frac{\langle v_t \rangle}{\sigma_\varepsilon} \right) \left(\frac{\partial \langle \varepsilon \rangle}{\partial X_j} \right) \right] + \frac{\langle \varepsilon \rangle}{\langle k \rangle}\left(C_{\varepsilon 1} P_k - C_{\varepsilon 2} \langle \varepsilon \rangle \right) \tag{18}$$

where $P_k = -\langle u_i' u_j' \rangle (\partial \langle u_i \rangle / \partial x_j)$ is the generation rate of turbulent kinetic energy. D_k and D_ε are the diffusion terms of the $\langle k \rangle$ and $\langle \varepsilon \rangle$ equations, respectively. The empirical constants such as C_1, C_2, $C_{\varepsilon 1}$, $C_{\varepsilon 2}$, C_μ, σ_k, and σ_ε are 1.8, 0.6, 1.44, 1.92, 0.09, 1.0, and 1.3, respectively [17].

2.3. Boundary conditions

2.3.1. Inlet and outlet conditions

For periodic fully developed flow, the periodicity of velocities and other turbulent quantities in the streamwise direction is used. The streamwise periodicity of mean velocity, temperature profiles and turbulent quantities is applied to the inlet and exit of one pitch module. The flow rate is determined by the pressure drop parameter λ through an iterative λ-correction method [18]. Guessed flow and temperature fields are used as initial values. For instance, turbulent quantities such as k were estimated from 1% to 5% U_{ref}^2 depending on the values of β and ε from the characteristic length and k at inlet. In addition, $\lambda = 129$, 147, 169, 216, and 216 corresponding to $\lambda = 44\%$, 32%, 22%, 10%, and 0% from the experiments, $\lambda = f\frac{1}{2}\rho U_{\text{ref}}^2/\text{De}$, is first adopted as a guessed value and then adjusted, due to numerical error, until the experimental Reynolds number 2×10^4 [9] is obtained. As the solution converges, the computed flow and temperature fields (mean and turbulent quantities) correspond to the experimental Reynolds number.

2.3.2. Near-wall treatment

Since the wall function treatment is employed in the near-wall region to bridge the viscous sublayer, the momentum and turbulent kinetic energy at all solid boundaries are evaluated from the logarithmic law of wall while the turbulent energy dissipation rate is determined from the local equilibrium. The nearest nodes from the wall are located within the interval $y^+ \doteq 18$–45. Constant heat fluxes are given at wall boundaries to simulate the heat transfer out of the solid parts to the fluids in the perforated passages due to heat conduction through the solid parts of the real three-dimensional (3-D) hole-type or slit-type perforated ribs adopted in the previous experimental studies.

2.4. Numerical method

By the use of the control-volume based finite difference method of Patankar [19], the governing equations were integrated over a finite number of control volumes covering the entire solution domain with each control volume containing a grid point. This integrated equation contains a convective term, an orthogonal diffusive term, and a source term including the nonorthogonal diffusive term. The convective terms of all equations, including the equations of scalar variables, were discretized by a third-order upwind scheme QUICK [20] and the orthogonal diffusive and source terms were discretized by the second-order central difference. For steady flow, the time derivative was discretized by a first-order accurate fully implicit method with a relatively large time step. As for handling the pressure–velocity coupling arising in incompressible flow equations, the PISO (pressure implicit with splitting of operators) [21] method was utilized for a stable and faster convergence at each time step for unsteady Navier–Stokes solutions. It involved one predictor step and a two-stage corrector scheme in each time step. The grid system was nonstaggered and the momentum interpolation method of Rhie and Chow [22] was adopted. The resulting set of algebraic equations was solved with the line-by-line TDMA (tridiagonal-matrix algorithm). The computed results were declared convergent when the maximum of individual and total sum of absolute cell residues in the entire domain for each dependent variable normalized by the respective inlet flux was less than a prescribed convergence criterion, typically values of 1×10^{-7} and 0.05%, respectively.

2.5. Code validation, grid independence and time step independence

Fig. 1 schematically shows the configuration for a channel with periodically perforated ribs for different rib open-area ratios. For code validation, Fig. 2 presents a comparison of the calculated and measured [23]

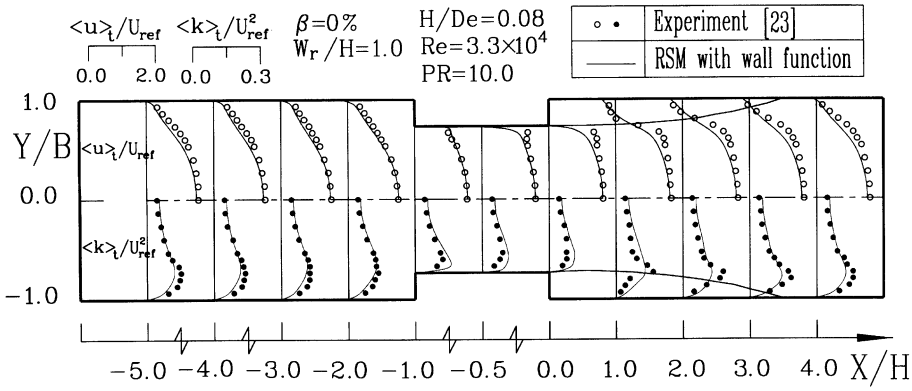

Fig. 2. Computed and measured streamwise time mean velocity and turbulent kinetic energy profiles at selected stations for channel with periodically square rib pairs.

streamwise time mean velocity and turbulent kinetic energy profiles at selected axial stations for $Re = 3.3 \times 10^4$, rib height-to-duct hydraulic diameter ratio (H/De) of 0.08, rib pitch-to-height ratio (PR) of 10, rib width-to-height ratio (W_r/H) of 1.0 and $\beta = 0\%$. Reasonable agreement is found between the calculated and measured data. The test computations were performed on a 152×92 grid. Additional runs for the coarser (102×62) and finer (202×122) meshes were undertaken for a check of grid independence. A comparison of the results of the two grid sizes, 152×92 and 202×122, shows that the maximum changes in the time mean axial velocity profiles are within 0.6%, which is relatively smaller than that found between 102×62 and 152×92 mesh sizes. The differences are so small that the accuracy of the solutions on a 152×92 grid size is deemed satisfactory. Four to five grid nodes were placed in the slits in y direction. The grid size near the wall was controlled to assure that the nearest nodes from the wall are located within the interval $y^+ \fallingdotseq 18$–45. The same constraint of y^+ range was applied to the regions near the front and rear edges of the ribs in the x direction.

The time step independence test was performed on three time steps: 1/100, 1/200, and 1/300 T_{cyc}. T_{cyc} is the vortex shedding period estimated from a Strouhal number of 0.2. The Strouhal number was based on the smallest height of the solid part of ribs and U_{ref}. The results show that no shedding phenomenon can be predicted in the present study. The flow becomes steady, even though it was simulated with an unsteady phase-averaged code. Mean velocity stands for long-time-averaged velocity.

2.6. Computed conditions

In this study, as a first step to simulate the complicated 3-D discrete perforations in the experiments of Hwang and Liou [3] and Liou et al. [9], the two-dimensional (2-D) slit ribs were adopted in the simulation. The rib open-area ratio was kept the same between the experiments and computations. The rib width-to-height ratio, rib height-to-duct height ratio ($H/2B$), and rib pitch-to-height ratio were 0.76, 0.17, and 10, respectively, and Reynolds number based on channel hydraulic diameter and bulk mean velocity was 2×10^4. The rib open-area ratio (β) was varied among 0%, 10%, 22%, 32%, and 44%. As shown in Fig. 1, three slits were chosen for the rib configuration according to the experiments [9], each slit with a height of $(\beta/3)H$. The solid part of the rib was divided into four regions, each with a height of $((1-\beta)/4)H$.

3. Results and discussion

3.1. Long-time-averaged mean flow pattern

The longitudinal mean flow pattern for $\beta = 44\%$, 32%, 22%, 10%, and 0% are presented in terms of velocity vectors and/or mean streamlines in Figs. 3–7, respectively. These figures reveal significant influence of the value of β on the mean flow pattern, especially the recirculating flow in the rib wake region. For $\beta = 44\%$ shown in Fig. 3, a larger part of fluid, about 4% of channel flow rate, located within a rib height distance from the bottom duct wall can flow through the rib slits and emerge from the rib rear edge in the form of multi-jets (will be elaborated on in the later text). Also note the presences of corner vortices (regions enclosed by null value of dimensionless stream function) ahead and behind the rib. As β decreases from 44% (Fig. 3) to 32% (Fig. 4), the amount of fluid passing through rib slits correspondingly decreases, about 3% of channel flow rate, hence not enough to provide the entrainment needs

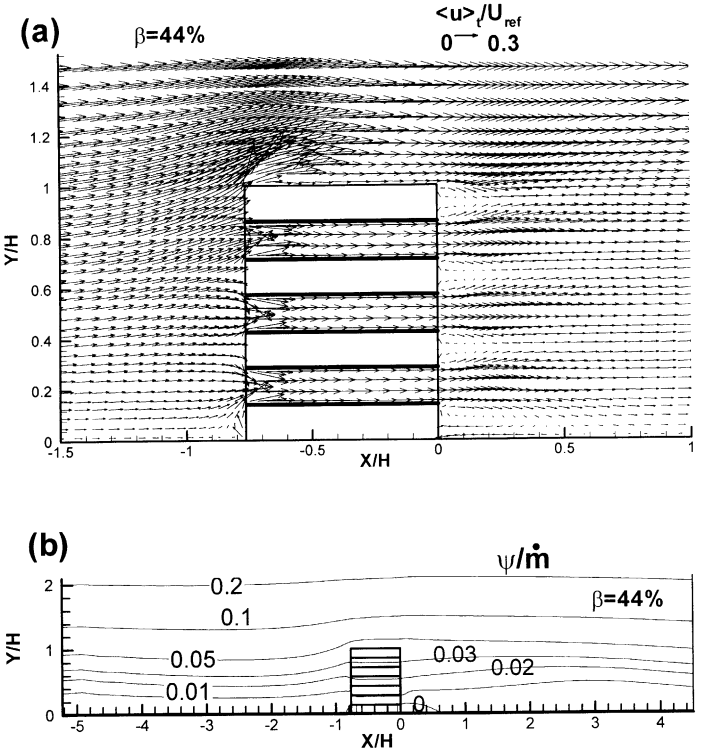

Fig. 3. (a) Time mean velocity-vector pattern near the slit-type perforated rib for $\beta = 44\%$. (b) Time mean streamline pattern in a pitch for $\beta = 44\%$.

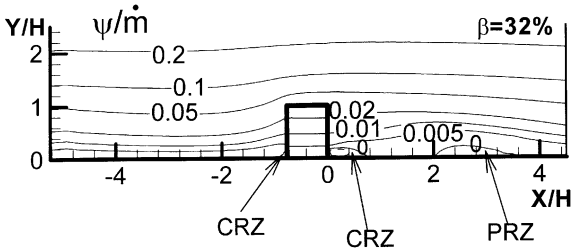

Fig. 4. Time mean streamline pattern in a pitch for $\beta = 32\%$.

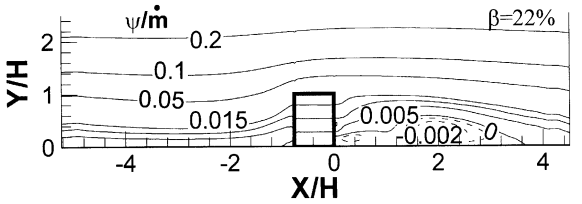

Fig. 5. Time mean streamline pattern in a pitch for $\beta = 22\%$.

of the separated shear layers (including the rib-top separated shear layer and the above-mentioned multi-jets), and the Coanda effect [24] becomes more significant. As a result, the flow bending increases to an extent such that

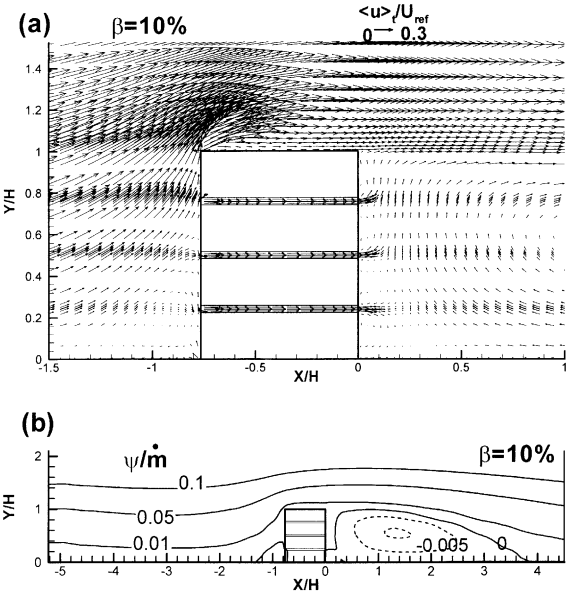

Fig. 6. (a) Time mean velocity-vector pattern near the slit-type perforated rib for $\beta = 10\%$. (b) Time mean streamline pattern in a pitch for $\beta = 10\%$.

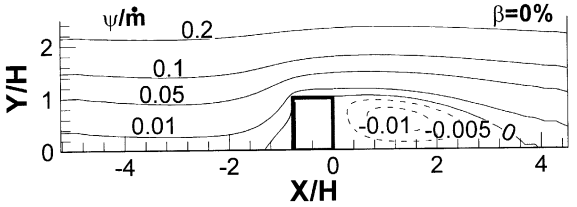

Fig. 7. Time mean streamline pattern in a pitch for $\beta = 0\%$.

the reattachment flow forms a small flow reversal region immediately upstream of the mean reattachment point $X_R/H = 3.6$. It is referred to as primary recirculation zone and measures $1.6H$ in length (L_R in Fig. 8) from $X/H = 2$ to 3.6, and $0.24H$ in height. Comparing Fig. 4 with Fig. 3, one finds the presence of a critical range of rib open area ratio ($32\% < \beta_{c1} < 44\%$) below which a flow reversal region appears upstream of the mean reattachment point. To find out the critical value, an additional run for $\beta = 38\%$ is performed. The flow pattern for $\beta = 38\%$ is similar to that for $\beta = 44\%$, but with a very small recirculation zone (length $L_R = 0.6H$, from $X/H = 2.7$ to 3.3, height $0.05H$). From the computations, the critical range of rib open area ratio lies in $38\% < \beta_{c1} < 44\%$. The first critical open area ratio range previously concluded by LDV measurements in a rectangular duct with hole-type perforated ribs [9] is $38\% < \beta_{c1} < 44\%$, just the same as that predicted by the present simulation. The β_{c1} range reported by Yamada and Osaka [8] from a low-speed flow visualization of boundary layer flow over a single hole-type perforated rib mounted on a flat plate is somewhat broader, $32.5\% < \beta_{c1} < 48.5\%$. The difference may be attributed to different rib arrangements and flow types between the two studies. No report of β_{c1} range for the horizontal broken-slit perforated ribs was given by Ref. [2].

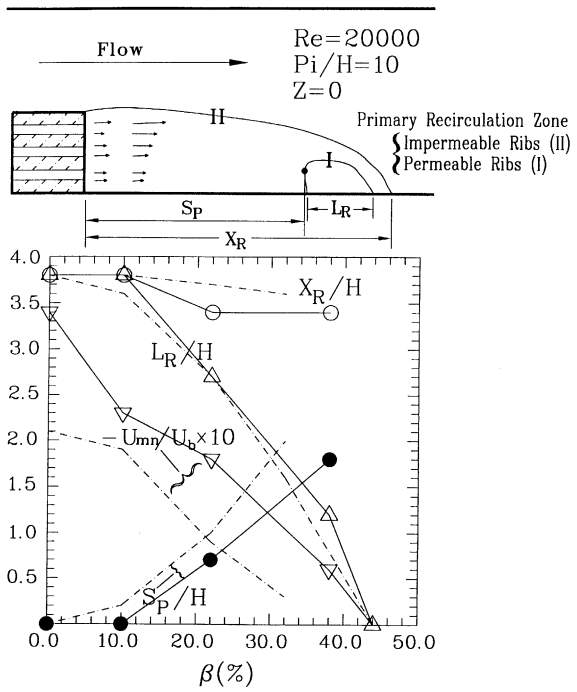

Fig. 8. Variation of reattachment length (X_R), primary recirculation zone length (L_R), stagnation point (S_P), and maximum negative axial mean velocity (U_{mn}) with rib open area ratio (β) for slit-type (dashdot line, present computation) and hole-type (symbols, LDV data [9]) perforated ribs.

For a still lower value of $\beta = 22\%$, the multi-jets become weaker and the size of reattachment induced recirculating flow region augments toward $X/H = 0$ and combines with the corner vortex at the rib bottom rear corner, as shown in Fig. 5. As β is continuously lowered to 10%, Fig. 6 indicates that the multi-jets behind the slit-type perforated ribs still exist, but with a drop of the maximum central jet exit velocity from 0.48 U_{ref} for $\beta = 44\%$ to 0.23 U_{ref} for $\beta = 10\%$. The recirculation zone is quite similar to that of impermeable ribs (Fig. 7, $\beta = 0\%$). There exists also a critical range of rib open area ratio ($\beta_{c2} < 10\%$) below which the slit-type perforated ribs are effectively impermeable and the flow pattern is typified by the well organized wake recirculating bubble and corner vortex at the rib bottom front corner. The laser holographic interferometry study of Hwang and Liou [3] reported the permeability limit of the hole-type perforated ribs as a function of β and Reynolds number. According to their critical curve, β_{c2} is 20% at $Re = 2 \times 10^4$ which is consistent with the LDV results of Liou et al. [9], $10\% < \beta_{c2} < 22\%$. Hence, the present computation for the slit-type perforated ribs shows a critical β_{c2} smaller than that of hole-type perforated ribs reported previously from the LHI and LDV measurements. The difference may be attributed to the different configurations of perforation used in the computations and measurements. The rectangular slits lead to a larger flow rate through the rib than the circular holes, which is similar to flow pass through the porous rib with equal porosity but different pore characteristic lengths [1]. No report of β_{c2} range for the horizontal broken-slit perforated ribs was given by Ref. [2].

Fig. 8 presents a summary of the related parameters characterizing the above discussed flow fields. The reattachment length X_R/H is found to be weakly dependent on the value of β. Once the multi-jets emerge from the rib rear edge (Fig. 6), $\beta > \beta_{c2}$, the primary recirculation zone is pushed downstream by the multi-jets. The larger the value of β, the stronger the multi-jets are and the further the primary recirculation zone or its front stagnation point S_p is pushed. Note that S_p measures from the rear side of the slit rib to the front stagnation point of the primary recirculation zone. Also bear in

mind that the reattachment length is a weak function of β. As a result, the length of the primary recirculation zone, L_R, decreases with increasing β and eventually vanishes at $\beta = 44\%$, as also shown in Fig. 3. Similarly, the absolute value of the nondimensionalized maximum negative streamwise mean velocity in the primary recirculation zone, $-U_{mn}/U_b$ in Fig. 8, decreases from 0.21 at $\beta = 0\%$ to only 0.03 at $\beta = 32\%$, and finally 0 at $\beta = 44\%$. Also shown in Fig. 8 is the results for the hole-type perforated ribs reported by Liou et al. [9]. Similar trends are found for these two types of rib perforation except those resulting from the difference in β_{c2} as addressed in the preceding paragraph.

The detailed axial mean velocity and turbulent kinetic energy profiles of the aforementioned multi-jets, featured by zigzags, and their streamwise evolution are depicted in Fig. 9(a) and (b) for the case of $\beta = 44\%$. The multi-jets interact each other due to the Coanda effect such that zigzags gradually become smooth as X/H is increasing up to $X/H = 1.2$. In the present study $X/H = 1.2$, where the zigzags in the mean velocity and turbulent kinetic profiles vanish practically, is defined as the effective jet length, designated as X_J, for $\beta = 44\%$, which is close to the LDV measured data [9], $X_J/H = 1.3$ for the hole-type rib perforations. It is also worth mentioning here that the multi-jets induced high k/U_{ref}^2 (Fig. 9(b)) contribute to the local heat transfer augmentation in the channel roughened by perforated ribs. Quantitatively, the multi-jets induced turbulent kinetic energy k/U_{ref}^2 range from 2% to 4% which are about seven to 13 times those in the smooth channel flow ($k/U_{ref}^2 = 0.03$–0.5% [25]) and two to four times those in the corresponding region of solid rib roughened channel flow ($k/U_{ref}^2 = 1$–3%).

3.2. Friction factor

Although the ribbed duct augments heat transfer, the presence of ribs increases the pressure loss. It is therefore worthwhile to study how the friction factor varies with rib's open area ratio. The friction factor in the spatially periodic region of the ribbed duct can be expressed as $f = [(-\Delta P/\Delta X) \cdot D_e]/(\rho \cdot U_b^2/2)$ where $\Delta P/\Delta X$ is the axial pressure gradient which is a part of the solution and iterated to satisfy the given flow rate and Reynolds number. Fig. 10 shows the presently computed and previously measured friction factor for perforated ribs as a function of β. The hole-type rib perforations

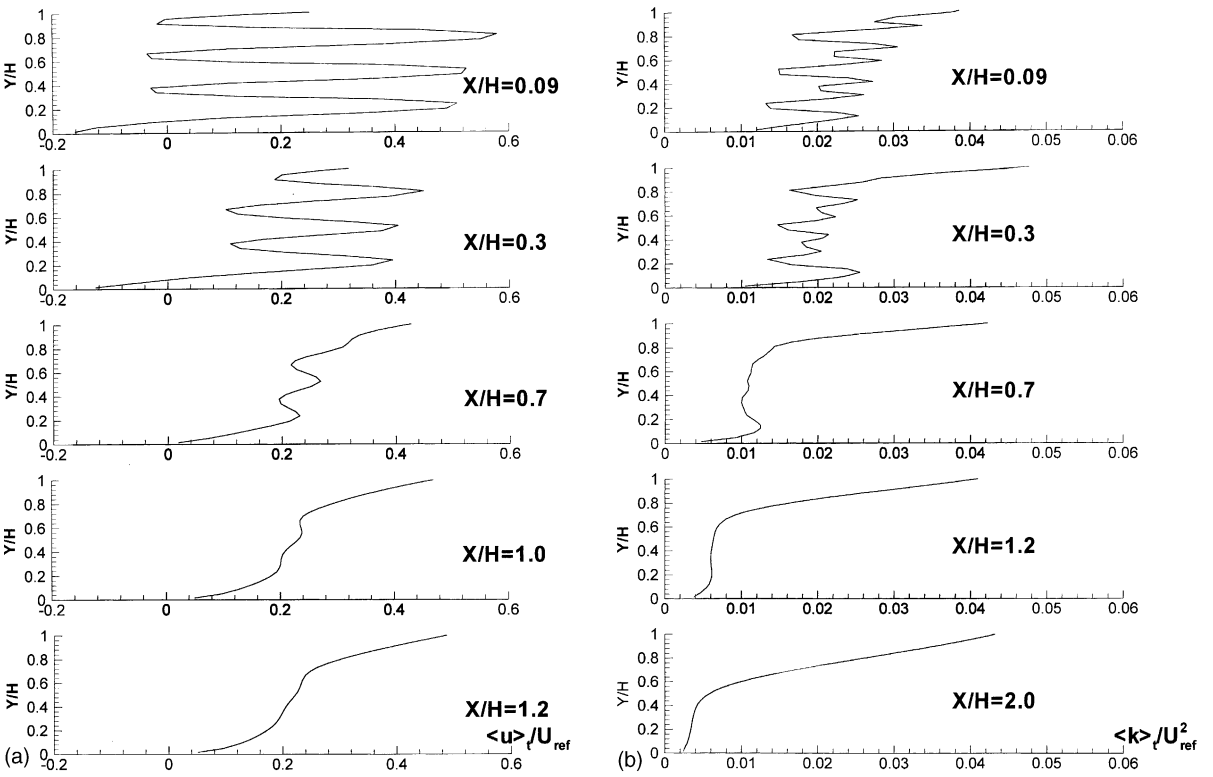

Fig. 9. (a) The zigzag multi-jet time mean velocity profiles at selected X/H locations for $\beta = 44\%$. (b) The zigzag multi-jet turbulent kinetic energy profiles at selected X/H locations for $\beta = 44\%$.

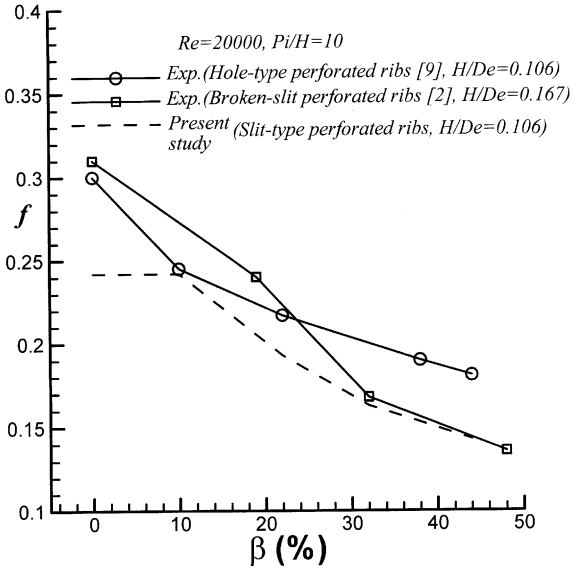

Fig. 10. Friction factors of calculated slit-type and measured hole-type perforated ribs as a function of β.

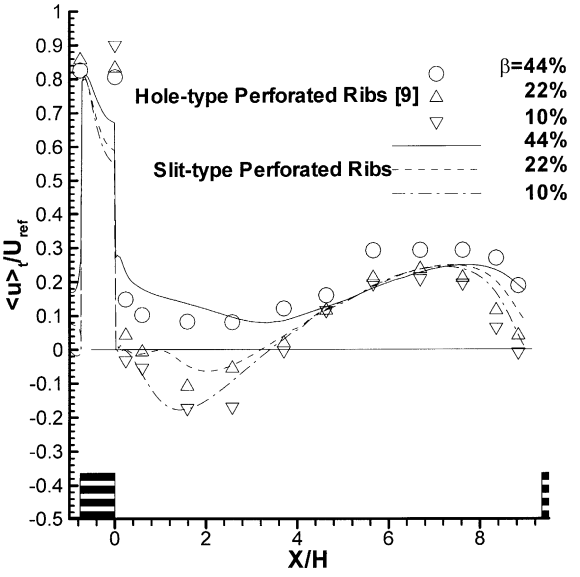

Fig. 11. Near-wall ($Y/H = 0.15$ for $X/H > 0$ and $Y/H = 1.15$ for $-1 < X/H < 0$) axial time mean velocity distributions for slit-type (computations) and hole-type (measurements [9]) perforated ribs with $\beta = 10\%$, 22%, and 44%.

of $\beta = 44\%$ can reduce the friction factor to about 60% of that of corresponding solid-type ribs ($f = 0.24$ at $\beta = 0\%$). The computed f for slit-type rib perforations are lower than the measured values for hole-type and broken-slit [2] rib perforations since the 2-D slit-type ribs are absent of side-wall and perforation-divider (or broken-slit-divider) frictions associated with the 3-D hole-type and broken-slit ribs experimentally investigated. Another reason is that the 2-D slits have larger pore characteristic length [1] than the circular holes although they have the same open area ratio. The computed f at $\beta = 0\%$ is equal to f at $\beta = 10\%$ for the slit-type perforated ribs since they are effectively impermeable for $\beta < 10\%$ and barely permeable at $\beta = 10\%$. Fig. 8 further shows that the maximum negative mean velocity $|-U_{mn}|$ only decreases slightly as β increases from 0% to 10% for the slit-type perforated ribs. All these observations support the results shown in Fig. 10, i.e. f at $\beta = 0\%$ equals f at $\beta = 10\%$. In contrast, Fig. 8 indicates that $|-U_{mn}|$ drops steeply as β increases from 0% to 10% for the hole-type perforated ribs. As a result, f decreases monotonically when β is increased from 0% to 10% for hole-type perforated ribs. The difference in measured f between the hole-type and horizontal broken-slit ribs is partly due to the differences in configuration and rib height.

3.3. Turbulent fluid flow and heat transfer

As mentioned in the Introduction, the heat transfer investigation of β effects for the hole-type perforated ribs performed by Hwang and Liou [3] concluded that $\beta = 44\%$ provided the best thermal performance under the same pumping power condition, i.e., while both heat transfer rate and friction loss are considered. For the slit-type perforated ribs, Fig. 11 depicts that $\beta = 44\%$ gives the highest positive convective mean velocity near the wall. In regard to the turbulent kinetic energy level, the pitch averaged k/U_{ref}^2 for the region between the ribs is found to be rather insensitive to the variation of β and has a value around $3.5 \pm 0.5\%$. Moreover, the friction factor results of Fig. 10 indicate that a minimum friction loss is associated with $\beta = 44\%$. These trends are similar to those reported for the case of hole-type perforated ribs as also included in Figs. 10 and 11. Furthermore, Fig. 12 shows the pressure contours for the three selected rib open-area ratios, $\beta = 44\%$, 22%, and 0%. As expected, larger rib open-area ratio leads to smaller value and region of negative pressure behind the rib, which corresponds to a smaller recirculation zone behind the rib. This observation is consistent with those shown in Figs. 3, 5 and 7. Consequently $\beta = 44\%$ should attain best heat transfer augmentation under the same pumping power condition for horizontal slit-type, horizontal broken-slit, and hole-type perforated ribs, as evidenced in Fig. 13 from the comparisons between solid, dashed, and dotted lines, between empty triangle and empty inverse triangle symbols, and between solid circle and empty square symbols, respectively. Note that for $\beta = 44\%$, the horizontal broken-slit perforated ribs (symbol: △) gives the best $\overline{Nu}_p/\overline{Nu}_s^*$ since their rib height is more than two times that of other cases. Also note

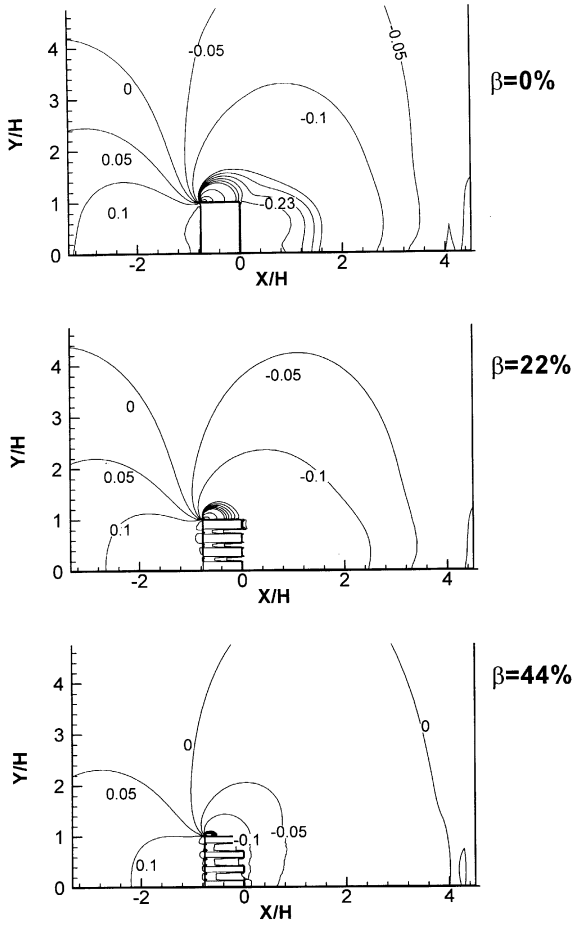

Fig. 12. The calculated pressure coefficient C_p contours for the three β values examined.

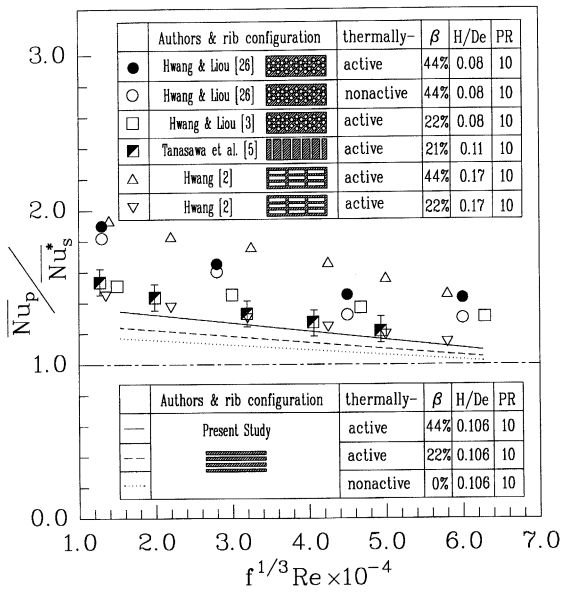

Fig. 13. Average Nusselt number ratio on the basis of pumping power for previous measurements and present study with $\beta = 10\%$, 22%, and 44%.

that the pitch-averaged Nusselt number Nu_p was obtained from the outer surfaces of the perforated ribs and the floor region between the consecutive ribs, if the results were compared with the measurements taken under thermally active condition. When the results were compared with the measurements performed under thermally nonactive condition, Nu_p was obtained from only the floor region between the ribs. It should also be mentioned that the periodic fluctuation, which has a definite effect on the heat transfer associated with solid-type ribs, is negligibly small due to the presence of slits of the perforated ribs examined. Hence, the heat transfer enhancement in the present study is addressed in terms of the long-time mean quantities.

Further observations can be made from Fig. 13. Lower Reynolds number attains higher $\overline{Nu}_p/\overline{Nu}_s^*$ for all cases listed in Fig. 13. In addition to the above-mentioned fluid dynamics and friction factors, the thermal activity of the rib itself plays an important role on the thermal performance of the ribbed duct [26]. For a given value of $\beta = 21$–22%, Fig. 13 depicts that $\overline{Nu}_p/\overline{Nu}_s^*$ is in the order of hole-type perforated ribs (symbol: □) > vertical-slit perforated ribs (symbol: ◩) > horizontal broken-slit perforated ribs (symbol: ▽) > horizontal-slit perforated ribs (dashed line) since the vertical heat conduction from the duct wall through the rib (fin effect) and heat transfer area (fin area) are the largest for the hole-type perforated ribs and the smallest for the horizontal-slit perforated ribs examined in the present work. For the case of the horizontal-slit perforated ribs, the vertical heat conduction is effectively blocked by the 2-D horizontal slits. Moreover, the shear layers of the horizontal slit-jets are primarily in the transverse direction whereas the shear layers of multi-jets behind the hole-type perforated ribs prevail in both transverse and spanwise directions. The shear-generated turbulent kinetic energy is thus larger for the hole-type perforated ribs as compared to the case of horizontal-slit perforated ribs. These observations explain the trend shown in Fig. 13.

4. Conclusions

Based on the results presented above for the rib open area ratio in the range of $0\% \leqslant \beta \leqslant 44\%$, some essential conclusions are drawn below.

1. For horizontal slit-type perforated ribs, there exists a critical range of rib open area ratio, $38\% < \beta_{cl} <$

44%, above which there is no primary recirculation zone behind the perforated rib. There exists a second critical range of rib open area ratio, $0\% < \beta_{c2} < 10\%$, below which the perforated ribs are practically impermeable.

2. For horizontal slit-type perforated ribs, below the first critical range of rib open area ratio, $38\% < \beta_{c1} < 44\%$, and above the second critical range of rib open area ratio, $0\% < \beta_{c2} < 10\%$, a primary recirculation zone appears in the region between ribs. The center of the primary recirculation zone moves upstream from near the reattachment point and its size extends toward the preceding rib, eventually combines with the corner vortex, as the rib open area ratio is decreased toward β_{c2}.
3. In general, both horizontal slit-type and hole-type perforated ribs demonstrate similar variations of fluid flow characteristics with the rib open area ratio except for the values of β_{c2}, $0\% < \beta_{c2} < 10\%$, and $10\% < \beta_{c2} < 22\%$ for the slit-type and hole-type perforated ribs, respectively. The reason for the difference in β_{c2} is that the rectangular slits have larger pore characteristic length than the circular holes although they have equal open area ratio.
4. The larger rib open-area ratio leads to smaller negative pressure behind the rib and, in turn, the smaller recirculation zone behind the rib. This fact together with the least friction loss and highest convective mean velocity for $\beta = 44\%$ illustrate that $\beta = 44\%$ of slit-type perforated ribs, as the case of hole-type perforated ribs reported previously, provides the best thermal performance under the same pumping power condition.
5. The hole-type perforated ribs provide the highest thermal performance under the same pumping power, followed by the vertical slit-type perforated ribs, and then the horizontal slit-type perforated ribs.

References

[1] T.M. Liou, S.H. Chen, Numerical simulation of turbulent heat transfer in a channel with a single porous rib, Chin. J. Mech. 11 (4) (1995) 319–326.

[2] J.J. Hwang, Heat transfer-friction characteristic comparison in rectangular ducts with slit and solid ribs mounted on one wall, Trans. ASME J. Heat Transfer 120 (1998) 709–716.

[3] J.J. Hwang, T.M. Liou, Augmented heat transfer in a rectangular channel with permeable ribs mounted on the wall, Trans. ASME J. Heat Transfer 116 (1994) 912–920.

[4] T. Tanasawa, S. Nishio, K. Takano, M. Tado, Enhancement of forced convection heat transfer in a rectangular channel using turbulence promoters, Proc. ASME–JSME Thermal Eng. Joint Conf. (1983) 395–402.

[5] T. Tanasawa, S. Nishio, S.K. Takano, High-performance surface for forced-convection heat transfer using novel turbulence promoters, ASME Paper 84-HT-69, 1984.

[6] K. Ichimiya, K. Mitsushiro, Enhancement of the heat transfer of wide temperature range in a narrow flow passage (effects of porous-type turbulence promoters in normal temperature range), in: R.K. Shah, E.N. Ganic, K.T. Yang (Eds.), Proceedings of Experimental Heat Transfer, Fluid Mechanics and Thermodynamics, Dubrovnik, Yugoslavia, 1988, pp. 659–664.

[7] K. Ichimiya, M. Katayama, T. Miyazawa, H. Kondoh, Experimental study on effects of a single porous-type roughness element in a parallel-plate duct, Exp. Heat Transfer 4 (1991) 319–330.

[8] H. Yamada, H. Osaka, Flow around a permeable rectangular plate standing vertically on the flat wall, 2nd report, effects of the aspect, the open area ratios, Trans. JSME 56 (546) (1992) 120–128.

[9] T.M. Liou, C.W. Kao, S.H. Chen, Flowfield investigation of the effect of rib open area ratio in a rectangular duct, Trans. ASME J. Fluids Eng. 120 (3) (1998) 504–512.

[10] J.J. Hwang, Turbulent heat transfer, fluid flow in a porous-baffled channel, J. Thermophys. Heat Transfer 11 (3) (1997) 429–436.

[11] G.J. Rowley, S.V. Patankar, Analysis of laminar flow, heat transfer in tubes with internal circumferential fins, Int. J. Heat Mass Transfer 27 (4) (1984) 553–560.

[12] O. Reynolds, On the dynamical theory of incompressible viscous fluids and the determination of the criterion, Phil. Trans. Roy. Soc. London Ser. A 186 (1895) 123–164.

[13] A.K.M.F. Hussain, W. Reynolds, The mechanics of an organized wave in turbulent shear flow, J. Fluid Mech. 41 (1970) 241–258.

[14] W. Rodi, On the simulation of turbulent flow past bluff bodies, J. Wind Eng. Ind. Aerod. 46–47 (1993) 3–19.

[15] B.E. Launder, G.J. Reece, W. Rodi, Progress in the development of a Reynolds-stress turbulence closure, J. Fluid Mech. 68 (1975) 537–566.

[16] T.J. Craft, B.E. Launder, New wall-reflection model applied to the turbulent impinging jet, AIAA J. 30 (1992) 2970–2975.

[17] W. Rodi, Turbulence Models and their Applications in Hydraulics, McGraw-Hill, New York, 1984.

[18] L.I. Shub, Calculation of turbulent flow and heat transfer in a tube with a periodically varying cross-section, Int. J. Heat Mass Transfer 36 (4) (1993) 1085–1095.

[19] S.V. Patankar, Numerical Heat Transfer and Fluid Flows, McGraw-Hill, New York, 1980.

[20] B.P. Leonard, A stable and accurate convective modelling procedure based on quadratic upstream interpolation, Comput. Meth. Appl. Mech. Eng. 19 (1979) 59–99.

[21] R.I. Issa, Solutions of the implicitly discretized fluid flow equations by operator splitting, J. Comput. Phys. 62 (1985) 40–65.

[22] C.M. Rhie, W.L. Chow, Numerical study of the turbulent flow past an airfoil with trailing edge separation, AIAA J. 21 (1983) 1525–1532.

[23] Y. Chang, Experimental Analysis of Turbulent Flows in a Rectangular Duct with Repeated Square-Rib Pairs, Master Thesis, NTHU, Taiwan, ROC, 1990.

[24] D.J. Tritton, Physical Fluid Dynamics, second ed., Oxford University Press, 1988.
[25] J. Laufer, The structure of turbulence in fully developed pipe flow, NACA TR 1174, 1954.
[26] J.J. Hwang, T.M. Liou, Heat transfer in a low-aspect ratio rectangular channel with thermally-active and nonactive perforated ribs, in: Proceedings of 12th National Conference on Mechanical Engineering, 1995, pp. 315–322.